

DISCRETE AND CONTINUUM MODELLING OF SILO DISCHARGE

C.J. Coetzee¹, A.H. Basson² and P.A. Vermeer³

Discrete and continuum modelling of silo discharge is presented. The Discrete Element Method (DEM) is used for discrete modelling and the Material-Point Method (MPM) for continuum modelling. MPM is a so-called particle method or meshless finite element method. Standard finite element methods have difficulty in modelling the complete discharge process unless remeshing is employed. The use of meshless methods overcomes this problem. Experiments are performed using a two-dimensional rectangular silo. Corn grains and sand are used as materials. A calibration process is proposed to determine the micro material properties needed for DEM simulations. The calibration process is based on experimental and numerical direct shear and compressions tests. Granular materials often exhibit rotational degrees of freedom associated with couple moments. To account for the rotation, the Cosserat polar continuum is used with MPM. DEM and MPM simulations are performed and the results of flow patterns and flow rates compared to experiments. It is concluded that both DEM and MPM can successfully model the total discharge process in terms of flow patterns and flow rates. A time study shows that if a relatively small number of particles are used in a DEM model, the computing times are comparable to that of MPM.

1. INTRODUCTION

Roughly one-half of the products and about three-quarters of the raw materials of the chemical industry are in the form of granular material that is usually stored in silos or bunkers. Although the silo is widely used, definite theories for the flow of material in silos are not available (Yang and Hsiau, 2001).

Rectangular silos have not been studied as often as circular silos, and relatively little detailed information

exists on pressure patterns which develop on their walls (Brown et al., 2000). Rectangular silos have advantages over circular silos when available space is limited and simplicity in construction is important. Brown et al. (2000) investigated the pressure on a model rectangular silo using a series of strain gauges and wall pressure sensors.

Yang and Hsiau (2001) investigated silo discharge using experiments and the Discrete Element Method (DEM). They used an "idealised" material: a single column of equally sized glass beads. The modelling of irregular shaped particles, such as sand or seed grains, is not addressed. They, however, obtained good results by comparing flow rates and flow patterns. Masson and Martinez (2000) used equally sized acrylic cylinders in experiments and compared the results to DEM simulations. Friction and contact stiffness proved to play a major role in the flow and the stress field during filling and discharging.

Martinez et al. (2002) investigated silo discharge using the Finite Element Method (FEM) with remeshing. The authors conclude that the remeshing introduces additional costs and meshless methods can avoid this inconvenience. Karlsson et al. (1998) used FEM based on the Eulerian frame of reference. The major disadvantage of this approach is that all boundaries are fixed. The upper free surface in a silo requires refilling to be fixed, and as a result it is not possible to simulate the complete discharging process. However, the redistribution of stresses when the flow develops is very fast, and the upper surface does not move much during this time. Thus, the Eulerian approach could be used to simulate only the initial stress transients.

In this paper, a plane strain flat bottomed silo is modelled using both discrete and continuum theories. The focus is mainly on flow patterns and flow rate. The flow pattern in a silo is of great importance when handling material that degenerates with time. Then it is important to achieve the first-in-first-out storage principle (Karlsson et al., 1998). DEM and a meshless finite element method, the Material-Point Method (MPM), were used to model the entire silo discharge. Commercial DEM software, *PFC^{2D}* (Itasca, 1999), was

¹ Department of Mechanical Engineering, University of Stellenbosch, Private Bag X1, Matieland, 7602, South Africa
Tel: +27 (21) 808 4239, Fax: +27 (21) 808 4958, E-mail: ccoetzee@sun.ac.za

² Department of Mechanical Engineering, University of Stellenbosch

³ The Institute of Geotechnical Engineering, University of Stuttgart, Germany

used. The MPM code was developed at the Department of Mechanical Engineering, University of Stellenbosch, in collaboration with the University of Stuttgart (Coetzee, 2004).

In the remainder of this section, a brief background is given on meshless methods with specific emphasis on MPM. The need for a polar continuum is introduced, and a brief background on the Cosserat polar continuum is given. In section 2, the experimental silo setup is presented. In section 3, the materials used and their properties are given. A DEM calibration process is proposed. The results from DEM and MPM (polar and nonpolar) are compared to experiments and presented in section 4.

1.1 Continuum Modelling

Over the last 25 years, the Finite Element Method has developed into the industry standard for solving a wide variety of solid mechanics problems. The problem of computational mechanics however grows more challenging. For example, in the simulation of manufacturing processes such as extrusion and molding, it is necessary to deal with extremely large deformations of the mesh while in computations of castings the propagation of interfaces between solids and liquids is crucial. In simulations of failure processes, propagation of cracks with arbitrary and complex paths needs to be modelled.

These problems are not well suited to conventional FEM. The underlying structure of FEM, which originates from its reliance on a mesh, is not well suited to the treatment of large deformations. The most viable strategy for dealing with large deformations is to remesh when the mesh becomes too distorted. This can, of course, introduce numerous difficulties such as the need to project between meshes in successive stages of the problem which can introduce additional computational errors (Belytschko et al., 1996 and Wiekowski, 2002). Remeshing can also be problematic where history-dependent material properties are present (Sulsky et al., 1995).

The objective of meshless methods is to eliminate at least part of the mesh structure by constructing the approximation entirely in terms of nodes (Belytschko et al., 1996). However in many meshless methods, recourse must be taken to meshes in at least parts of the method. Thus, it becomes possible to solve large classes of problems (e.g. large deformations, cracks and discontinuities) that are very awkward with mesh-based methods. Although meshless methods originated about twenty years ago, little research effort has been devoted to them until recently. For a summary of the different meshless methods currently available and a short history, see Coetzee (2004).

Particle meshless methods can be characterised as methods where the solution variables are attributed to Lagrangian point masses instead of computational cells (Benson, 1992). The particle methods were originally used in fluid dynamics.

Sulsky et al. (1995) developed a particle method called the Material-Point Method (MPM). MPM is applicable to solid mechanics and can be used to model dynamic impact, penetration and large deformations. MPM uses two discretisations of the material, one based on a computational mesh and the other based on a collection of material points or *particles*. This approach combines the advantages of Eulerian and Lagrangian descriptions of the material while avoiding the shortcomings of each.

The equations of motion are solved in a Lagrangian frame on a computational grid, using standard finite element methods. Convection is modelled by moving the material points in the computed velocity field. Each material point carries its material properties without error while it is moved. Material points may cross over from one element to another. Since all the state variables are assigned to the material points, the information carried by these points is enough to characterise the flow and the grid carries no permanent information. Thus, the grid can be discarded and reconstructed for computational convenience at each time step.

The MPM formulation results in an automatic no-slip condition between different bodies. Bardenhagen et al. (2000) developed an algorithm that precludes interpenetration of different bodies, but allows frictional slip at the contacting boundary nodes. This contact model is used to model the frictional interface between the silo walls and the granular media. See Appendix A for a more detailed description of MPM.

In granular materials the discreteness of the system is often important and rotational degrees of freedom and couple moments are active, which might require enhanced theoretical approaches like polar continua (Herman, 1999). In polar continuum theories, the material points are considered to possess orientations. A material point has three degrees-of-freedom for rigid rotations, in addition to the three classic translational degrees-of-freedom. Eringen (1999) describes polar continua in detail. The Cosserat continuum is the most transparent and straightforward extension of classic or nonpolar continuum models and was proposed by E. and F. Cosserat in 1909 (de Borst, 1991). The nonpolar constitutive laws must be adapted to include the rotational degrees-of-freedom which leads to new laws such as polar elasticity and polar plasticity. The rotations are induced by couple stresses within the continuum. The presence of couple stresses result in a

stress tensor which is no longer symmetric, as in the case of a nonpolar continuum. See Appendix B for a more detailed description of the Cosserat continuum.

In this paper, both the classic (nonpolar) and the Cosserat (polar) continuum are used with MPM.

1.2 Discrete Modelling

Discrete Element Methods are based on the simulation of the motion of granular material as separate particles. DEM was first applied to soils by Cundall and Strack (1979). Calculations performed during a DEM simulation alternate between the application of Newton's second law to the particles and a force-displacement law at the contacts, Figure 1.

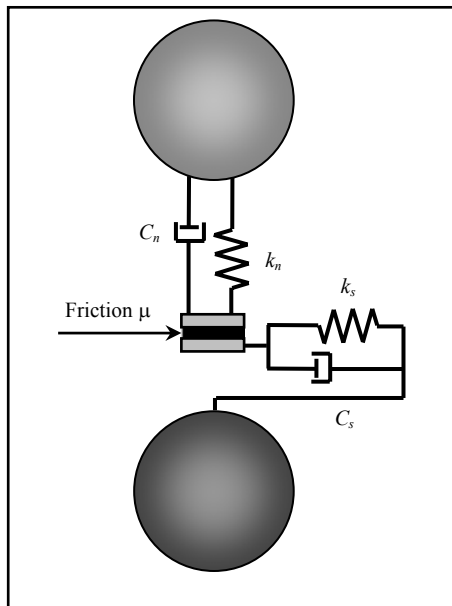


Figure 1. DEM contact model

Using the soft particle approach, each contact is modelled with a spring in the normal and tangential direction. Different damping models are available such as viscous damping and mass damping (Itasca, 1999). Frictional slip is allowed in the tangential direction. The particles are allowed to overlap and the amount of overlap is used in combination with the spring stiffness to calculate the contact force. DEM has the advantage that it can easily be used for the simulation of granular flow subjected to large deformations and free boundaries.

The main problem with DEM is specifying the micro properties (spring stiffness, friction coefficient, damping values). The micro properties should be specified such that the flow of thousands of particles behaves in the same way as the real granular material (Franco et al., 2005). Laboratory experiments (e.g.

shear tests, biaxial tests and oedometer tests) or in-situ tests (Asaf et al., 2005) are necessary to determine these properties before any useful modelling and predictions can be made. A calibration process is proposed and tested in this paper.

2. EXPERIMENTAL SETUP

A model silo was built to investigate the flow of material out of a plane strain flat bottomed silo. The focus was mainly on flow patterns and flow rate. The model silo used for the experiments had dimensions of 310 mm wide, a maximum fill height of 600 mm and a depth (out-of-plane) of 730 mm. All the sides were constructed of glass and the opening width could be varied. The depth to width ratio of the silo was high enough for the flow to be two-dimensional. It was assumed that all silces (into the plane) have the same in-plane velocity profile. The results confirmed this assumption.

The silo was filled in the same way used by Brown et al. (2000): A hopper was suspended above the silo and its door (200mm \times 200 mm) opened until the silo was filled. The top surface was then carefully levelled. Coloured grains were used to create layers within the material which could be used to compare flow patterns.

During discharge, the mass of the material within the silo was measured by suspending the silo from a load cell. The question however arises whether the measured mass of the material during discharge is a true representation of the flow rate. Close to the silo opening the free falling material will not contribute to the measured weight although the material is still within the silo. The acceleration and deceleration of the material as it flows in the silo will also create dynamic effects. The flow rate is defined as the rate at which material flows through the silo opening, measured in $\text{kg}\cdot\text{s}^{-1}$. The results of the DEM simulations were used to clarify this point (see section 4).

3. MATERIAL AND DEM CALIBRATION

Two types of material were used: corn and sand. Silo experiments were performed using both materials, DEM simulations with only corn and MPM simulations with both corn and sand. The corn grains were relatively large and each grain could be modelled using DEM which is impossible to do with sand.

3.1 Corn Properties

Both the micro- and macro properties were needed for DEM and MPM simulations respectively. Very few researchers have tried to determine the micro-parameters experimentally. Vu-Quoc (2000) measured the coefficient of restitution in soybeans by performing

simple drop tests from various heights. Data from high-speed video recordings was used to determine the particle properties. Tanaka (2000) conducted bar penetration tests and compared the results with those obtained from DEM simulations. The material density could be measured, but the contact stiffness was chosen without any experimental validation. By comparing the movement of the particles during the experiment with the movement during the simulation, while different particle friction coefficients were used, the friction coefficient that gave the best results could be determined.

Recently, Franco et al. (2005) proposed a method to determine the micro properties for modelling soil-bulldozer blade interaction. In their approach, the particle friction coefficient and stiffness are determined from energy principles and direct shear tests (experiments and numerical). The method, however, can result in more than one combination of friction and stiffness values. Asaf et al. (2005) proposed an in-situ method for determining the micro properties. Their method is based on wedge penetration tests and a non-linear optimisation scheme.

In this section, a new process for determining micro parameters for frictional material is proposed. There is assumed to be no cohesion or adhesion at particle-particle and particle-wall contacts respectively. The parameters to be determined are the particle size, particle shape, particle density, particle stiffness, particle-particle friction coefficient and particle-wall friction coefficient. The particle size, shape and density are first determined and modelled and then shear tests and compression tests are used to determine the particle stiffness and friction coefficient.

3.1.1 Particle size and shape

The particle size was chosen so that it roughly represented the physical shape and size of the corn grains. Particles were constructed by forming clumps. Clumps, PFC^{2D} (Itasca, 1999), can be formed by adding two or more particles (discs) together to form one rigid particle, i.e. particles comprising the clump remained at a fixed distance from each other. Particles within a clump can overlap to any extent and contact forces are not generated between these particles. Clumps can not break up during simulations regardless of the forces acting upon them. Figure 2 shows the “tear-drop” shape of the grains and the equivalent DEM clump used. The diameter of the disc shaped particles used in the simulations was chosen from a uniform distribution within the range shown in the figure.

Although the grain shapes could be modelled more accurately by using more than two particles in a clump,

the representation chosen was thought to be accurate enough and computationally efficient.

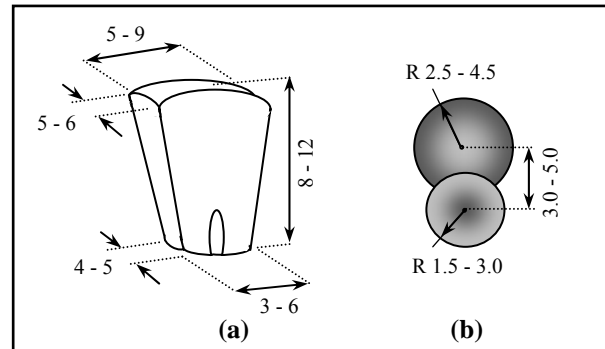


Figure 2. (a) Physical grain dimensions and (b) DEM grain model. Dimensions in [mm]

3.1.2 Particle density

The average (bulk) material density was measured by filling a cylindrical container with material. The container with material was weighed and the internal dimensions of the container measured to calculate the volume. The average density was defined as the total material mass divided by the volume filled by the material.

In the model, all the particles were given an initial density (solid density) slightly higher (15%) than the measured average density. The assembly of particles was then allowed to reach static equilibrium and the average density calculated using the total mass of all the particles and the total volume filled by the assembly of particles. Using an iterative procedure, the density of all the particles was changed until the average density was within 0.1% of the measured value. This could be obtained within three to four iterations. After each iteration, the assembly of particles was allowed to reach a static equilibrium state.

3.1.3 Direct shear tests

Shear failure occurs when shear stresses set up in the material exceed the maximum shear resistance that the material can offer, i.e. its shear strength. The shearbox test is the simplest, the oldest and the most straightforward procedure for measuring the shear strength (internal friction angle) of granular material.

A shearbox was used to experimentally determine the corn internal friction angle and the friction angle between the corn and glass (silo walls). The box had dimensions of 375 × 375 mm with a total height of approximately 175 mm and was large enough for testing particles up to 12 mm in size (Head, 1998). The normal stresses imposed during the tests were

chosen to be within the range experienced during silo discharge. A numerically equivalent DEM model with the same dimensions as the physical apparatus was constructed and tests were performed under the same conditions. The average shear stress between 2.1% and 4.8% strain (8 and 18 mm of displacement) was used to calculate the friction angle, which was defined as the average shear stress divided by the average normal stress, Figure 3.

A series of shear tests were performed using a range of particle stiffness and friction coefficient values. The shear simulations showed that the internal friction angle depended on both the particle stiffness and friction coefficient, especially in the low stiffness range.

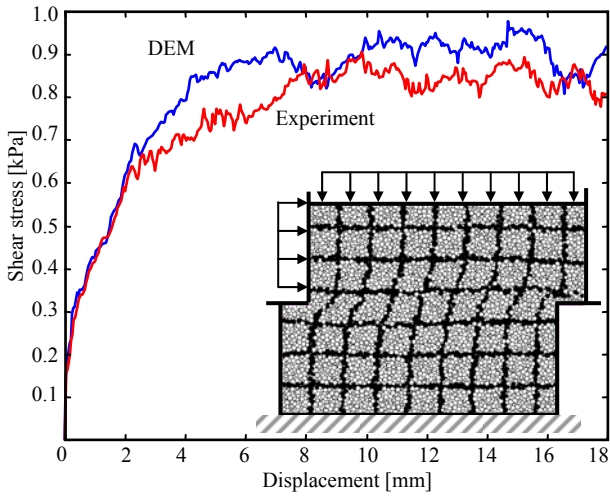


Figure 3. Typical shear test result

Although the ratio of particle normal to particle tangential stiffness, k_n/k_s , has an influence on the materials Young's modulus and Poisson's ratio, PFC^{2D} (Itasca, 1999), this ratio was taken equal to one, i.e. the particle normal and tangential stiffness were assumed to be the same. Poisson's ratio given by a 2-D biaxial simulation can strictly not be compared with laboratory-measured values since conditions in a 2-D biaxial test are neither plane strain nor plane stress, PFC^{2D} (Itasca, 1999). Consequently, Poisson's ratio was not used in the calibration process.

The shear test results are shown in Figure 4. From the figure, it is clear that both the particle stiffness and friction coefficient have an influence on the material internal friction angle, ϕ .

For stiffness values below 100 kN/m the internal friction angle is strongly dependent on the particle stiffness, but for higher stiffness values the dependence decreases, and more so for lower friction coefficients. Thus, the direct shear test can not be used to determine a unique set of parameters. It is clear from Figure 4

that more than one combination of the particle friction coefficient and stiffness values can result in an internal friction angle similar to the measured value (indicated by the dotted line). Another test, the confined compression test, is used in the next section to determine the unique set of parameters. The friction angle with glass and steel was measured by replacing the lower part of the shearbox with a glass and steel sheet respectively.

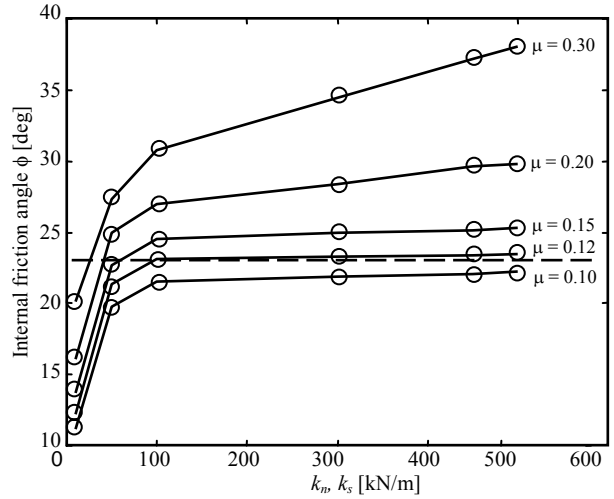


Figure 4. The effect of particle stiffness and friction on the material internal friction

3.1.4 Confined compression test

In the confined compression test (also called the oedometer test), stress is applied to the specimen along the vertical axis, while strain in the horizontal directions is prevented. Shear stresses and shear strains as well as compressive stresses and volume changes occur in this test, but since the material is prevented from failing in shear, compression is the dominant source of strain.

Usually this test is used to determine soil consolidation ratios. Here it is used to determine the elasticity of the material, similar to a uniaxial tensile test. There are, however, some differences between the confined compression test performed here and a uniaxial tensile test. During a uniaxial tensile test, stress is applied in the axial z-direction. There is no stress in the x- and y-directions, but strain in all three directions, ϵ_x , ϵ_y and ϵ_z . Young's modulus of elasticity is defined as

$$E = \frac{\sigma_z}{\epsilon_z} \quad (1)$$

During confined compression, the direct strain in the x- and y-directions is constrained to be zero. This has the result that normal stresses develop in the x- and y-directions. It can be shown that the relation between the *confined* Young's modulus E' and the usual Young's modulus E , is given by

$$E = E' \left(\frac{(1+\nu)(1-2\nu)}{1-\nu} \right) \quad (2)$$

where ν is Poisson's ratio and E is given by Equation 1.

The experiments were performed with a 250 mm diameter cylinder and a specimen height of 80 mm. Side friction will always play a role in this test and therefore it had to be included in the numerical model. The wall friction was set to the specific material-steel friction coefficient. Figure 5 shows typical experimental results obtained from unloading and reloading (hysteresis).

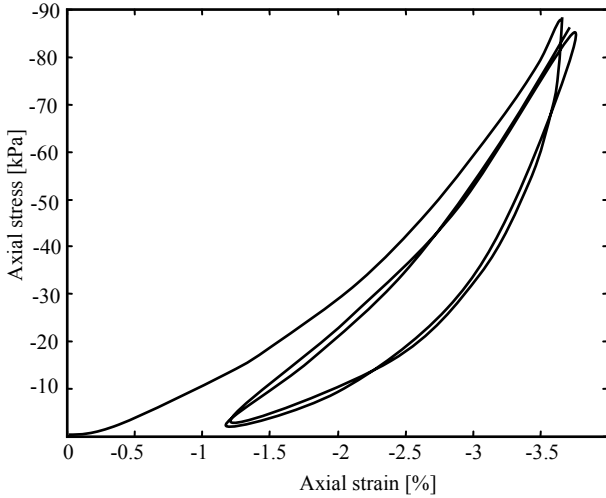


Figure 5. Experimental results from confined compression test

Only a portion of the strain that occurred during initial loading was recovered during subsequent unloading. The strains that resulted from sliding between particles were largely irreversible. The rebound upon unloading was caused by the elastic energy stored within the particles, as the assembly was loaded. However, there could be some reverse sliding between particles during unloading. Only a small amount of permanent strain resulted from the next two cycles. All experiments were performed at low compression rates to avoid any dynamic effects, i.e. quasi-static conditions were assumed. Figure 6 shows the numerical result with little to no hysteresis.

Experiments and simulations were stopped after three cycles. The second and third cycles followed a stable hysteresis loop. These stable cycles were used to determine the stiffness of the system of particles. The confined Young's modulus was calculated as

$$E' = \frac{\sigma_{80} - \sigma_{10}}{\varepsilon_{80} - \varepsilon_{10}} \quad (3)$$

where σ_{80} is an axial compression stress of 80kPa and ε_{80} the equivalent strain, etc. A series of simulations, each with different particle stiffness and friction values,

were performed. The results are summarised in Figure 7.

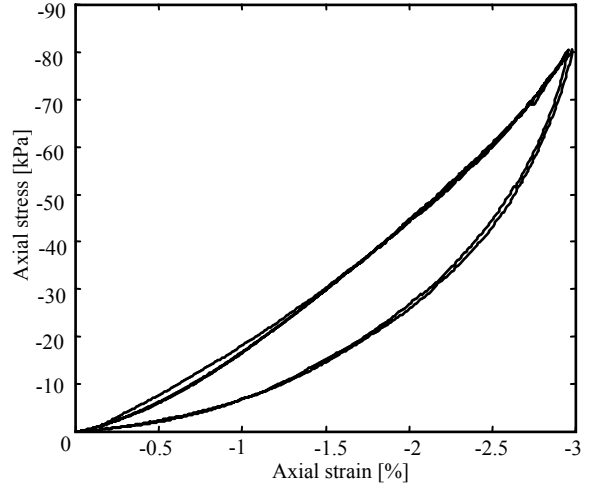


Figure 6. Numerical results from confined compression test

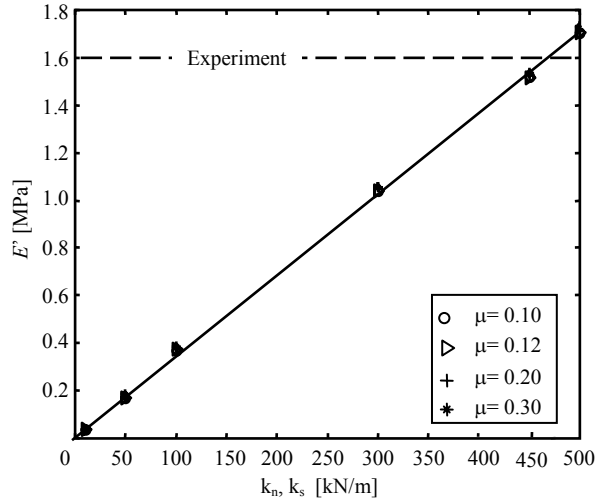


Figure 7. Effect of particle stiffness and particle friction on the confined stiffness

It was found that the friction coefficient had little to no effect on the system stiffness and a linear relation existed between particle stiffness and the confined Young's modulus.

With both the shear test and compression test results available, a unique set of micro parameters could be determined. The compression test showed to be independent of the particle friction within the range tested. A particle stiffness of 450 kN/m resulted in a confined Young's modulus close to the measured value (Figure 7). With the stiffness known, the shear results (Figure 4) could be used to determine the particle friction coefficient. A value of $\mu = 0.12$, resulted in an internal friction angle close to the measured value of $\phi = 23^\circ$.

3.1.5 Angle of repose

With the particle size, shape, stiffness and friction known, the angle of repose ϕ_r was determined experimentally and numerically as a final test. Figure 8 shows a simulation after it reached equilibrium. One thousand particles were dropped from a fixed height and allowed to settle under gravity. The simulations corresponded well to experimental measurements. It is also known that for frictional cohesionless granular material, the angle of repose is a good indication of the internal friction angle (Lambe and Whitman, 1969).

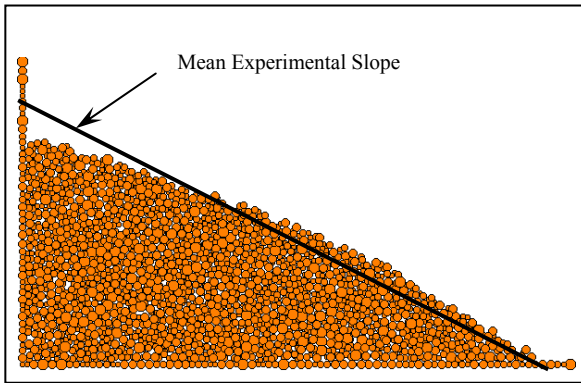


Figure 8. Angle of repose

3.1.6 Summary of corn properties

Table 1 summarises the corn material properties. The measured values were determined experimentally. The DEM macro properties were obtained numerically using the calibrated micro properties. The values of the angle of repose, average density and material-steel friction coefficient correspond well to the values measured by Reimbert (1976).

Macro Property	Measured	DEM
Internal friction angle, ϕ	23.0°	23.4°
Angle of repose, ϕ_r	25°±2°	24°±1°
Average density, ρ	778 kg/m ³	778 kg/m ³
Bulk modulus, E'	1.60 MPa	1.52 MPa
Material-steel friction, ϕ_s	14°	14°
Material-glass friction, ϕ_g	12°	12°
Calibrated Micro Properties		
Particle stiffness, $k_n = k_s$	450 kN/m	
Particle density, ρ_p	855 kg/m ³	
Particle friction	0.12	

Table 1. Calibrated corn material properties

In addition to the measured material properties given in Table 1, the properties given in Table 2 were also used for MPM modelling. The modulus of elasticity was calculated using Equation 2. The values for Poisson's ratio and the dilatancy angle were assumed.

Property	Value
Bulk modulus, E	1.44 MPa
Poisson's ratio, ν	0.2
Dilatancy angle, ψ	2°
Cohesion, c	0 Pa
Cosserat shear modulus, $G_c = 2G$	1.20 MPa
Characteristic length, l	10 mm
Moment of inertia, $J = 0.5(0.5l)^2$	12.5·10 ⁻⁶ m ²

Table 2. Macro properties of corn used in MPM simulations

A Drucker-Prager constitutive model (FLAC, 1998) was used for nonpolar MPM modelling and a polar Drucker-Prager model (Tejchman, 1997) for polar MPM modelling. The corn grains had an average size of more or less 10 mm. The characteristic length used in the polar continuum, assumed these values (Tejchman, 1997). The moment of inertia was calculated by assuming a cylinder with a diameter equal to the internal length. The moment of inertia is used to calculate the Cosserat angular momentum per unit mass $h_i^c = J\omega_3^c$ (see Appendix B).

3.2 Sand Properties

The sand was only modelled using MPM, thus only the macro properties were needed. Dry graded silica sand was used with the following main constituents: SiO₂ = 98% and Fe₂O₃ = 0.18%. A shear test and a confined compression test were used to determine the sand friction angle and elastic modulus respectively. The bottom half of the shear box was replaced by a glass panel to measure the friction between the sand and glass. Poisson's ratio was taken to be $\nu = 0.2$. The dilatancy angle was not measured and values of 2° and 5° were used. The effect of the different dilatancy angles on the material flow is described in the results. The sand properties are summarised in Table 3. The same constitutive models used for corn were used to model the sand.

4. RESULTS

In the DEM model, the silo was filled following the experimental procedures. In the MPM models the material was created layer-by-layer and allowed to reach an equilibrium state after each layer was added.

Equilibrium was achieved by adding damping to the system (FLAC, 1998). During discharge no damping was applied and energy dissipation occurred through material plasticity.

In the MPM models a symmetry plane was used and friction applied at the remaining walls. No polar rotations were allowed at the walls which is the case for relatively smooth walls (Tejchman, 1997). The 40×50 rectangular mesh had elements of size $3.875 \text{ mm} \times 10 \text{ mm}$. Time steps of $\Delta t = 5 \times 10^{-5}$ seconds and $\Delta t = 2 \times 10^{-5}$ seconds were used for the modelling of corn and sand respectively. In the DEM models no symmetry plane was used and as a result the flow patterns are not perfectly symmetric.

Property	Value
Internal friction angle, ϕ	32°
Average density, ρ	1286 kg/m^3
Bulk modulus, E	21.5 MPa
Poisson's ratio, ν	0.2
Dilatancy angle, ψ	$2^\circ, 5^\circ$
Cohesion, c	0.9 kPa
Material-glass friction, ϕ_g	18°
Cosserat shear modulus, $G_c = 2G$	17.9 MPa
Characteristic length, l	1 mm
Moment of inertia, $J = 0.5(0.5l)^2$	$12.5 \cdot 10^{-8} \text{ m}^2$

Table 3. Macro properties of sand used in MPM simulations

Figure 9 shows the flow of corn out of the silo with the silo opening $w = 45 \text{ mm}$ and the initial fill height $h = 500 \text{ mm}$. The experimental, polar MPM, nonpolar MPM and DEM results are shown at increments of two seconds, up to seven seconds. There is a good agreement between the DEM and experimental results regarding flow patterns. It can, however, be seen that the DEM discharge rate is higher. Qualitatively, the nonpolar MPM flow patterns and flow rate compare well to the experiment. Polar MPM shows a higher flow rate and there is a definite difference in the flow patterns compared to nonpolar MPM. To make a quantitative comparison of the flow patterns is difficult. The flow rate can, however, be compared quantitatively.

The mass of the material within the silo was measured by suspending the silo from a load cell. The question however arises whether the measured mass of the material during discharge is a true representation of the flow rate. Close to the silo opening the free falling material will not contribute to the measured value

although the material is still within the silo. The acceleration and deceleration of the material as it flows in the silo will also create dynamic effects. The flow rate is defined as the rate at which material flows through the silo opening measured in $\text{kg} \cdot \text{s}^{-1}$.

The results of the DEM simulations were used to clarify this point. Figure 10 shows the two methods of calculating the mass of material within the silo. 1) The *mass method*: simply add up the mass of all the particles above the silo opening at each time step. 2) The *load method*: add the resultant vertical force (converted to mass in kg) of all the walls at each time step. The *load* approach is similar to the experimental approach. From the figure it can be seen that the resultant vertical force on the silo walls show high fluctuations due to the collisions between the particles and the walls. The result from the *mass method*, however, is a good fit to the result from the *load method*. It can be concluded that the measured values are a good representation of the material mass in the silo.



Figure 9. Corn flow patterns with the silo opening $w = 45 \text{ mm}$

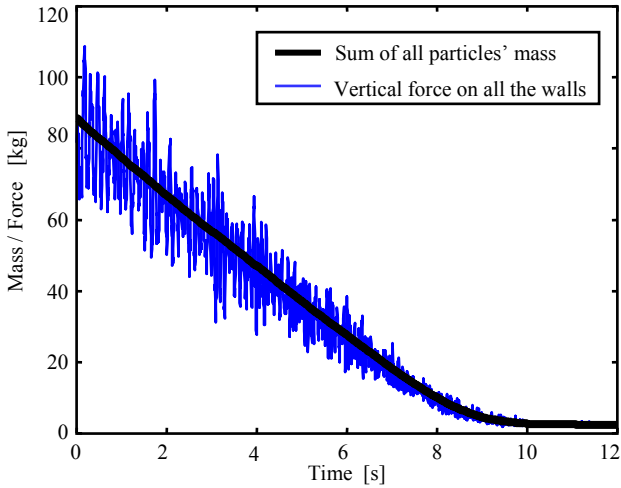


Figure 10. Comparison of the two methods for calculating mass flow out of the silo using DEM, $w = 45$ mm

Figure 11 shows the corn mass within the silo as a function of time for two openings: $w = 45$ mm and $w = 80$ mm and the initial fill height $h = 500$ mm. For both openings, DEM predicts a higher flow rate than the measured rates. With $w = 45$ mm, nonpolar MPM predicts a higher flow rate and with $w = 80$ mm a lower flow rate compared to the experiment. Polar MPM predicts a higher flow rate compared to the experiment for both openings and the results are in close agreement with the DEM results. Figure 12 shows the sand mass within the silo as a function of time with $w = 45$ mm and the initial fill height $h = 550$ mm. Since the dilatancy angle could not be measured, two values $\psi = 2^\circ$ and $\psi = 5^\circ$ were used. As expected, with an increase in dilatancy angle there is a decrease in mass flow from the silo. The results with $\psi = 2^\circ$ are closer to the measured values. The dilatancy angle $\psi = 2^\circ$ is typical for loose sand (Vermeer, 1984). As in the case with corn, polar MPM predicts a higher flow rate than nonpolar MPM.

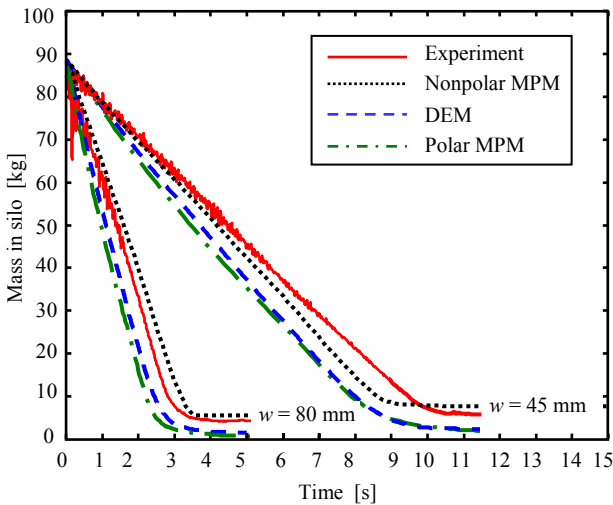


Figure 11. Corn mass in the silo versus time for $w = 45$ mm and $w = 80$ mm

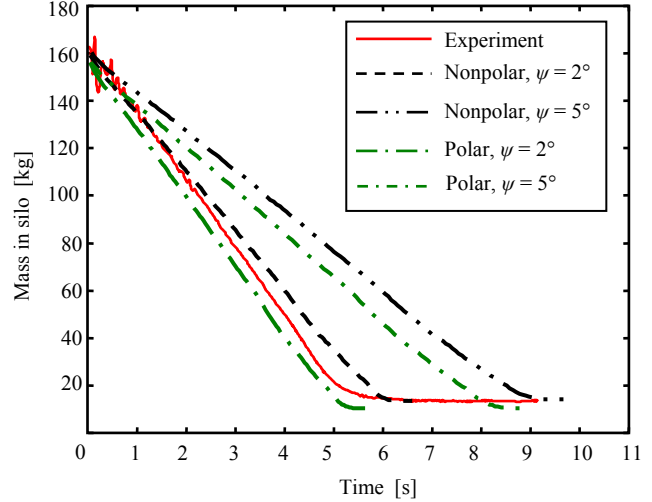


Figure 12. Sand mass in the silo versus time for $w = 45$ mm

Figure 13 shows the results from a mesh convergence study using corn, $w = 45$ mm and a symmetry plane. The mass flow rate was based on the steady state flow rate as seen in Figure 11. The mesh sizes used are indicated in the figure and the results support the choice of 40×50 elements.

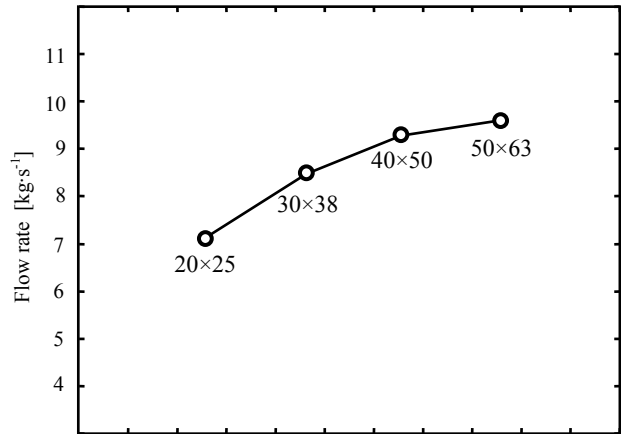


Figure 13. Convergence in mass flow with mesh refinement

5. COMPUTING TIMES

DEM, nonpolar MPM and polar MPM simulations were used to model corn flowing from the silo. The run time to model the first ten seconds of silo discharge ($w = 45$ mm) is shown in Table 4 for each simulation. The number of particles/material points used are indicated as well as the initial number of degrees-of-freedom, DOF. The simulations were all run on a Pentium IV 2.4 GHz. The DEM model had 5348 circular particles (disks) making up 2674 clumps. Four MPM models were used: a polar continuum with a symmetry plane and the full geometry, a nonpolar continuum with a symmetry plane and the full geometry. The full geometry ($310 \text{ mm} \times 500 \text{ mm}$) was divided into $80 \times 50 = 4000$ elements and the geometry

with the symmetry plane (155 mm×500 mm) was divided into 40×50 elements. A time step of $\Delta t = 5 \cdot 10^{-5}$ seconds was used in all the simulations including DEM.

When a symmetry plane is used, the nonpolar and polar MPM methods are both quicker than the DEM simulation by 39% and 9.3% respectively. When the full geometry is modelled, the number of degrees-of-freedom is more or less doubled and the simulations slower by 134% and 266.5% compared to the DEM simulation respectively. Polar MPM is slower than nonpolar MPM by more or less 50% which is expected because of the three degrees-of-freedom compared to the two degrees-of-freedom per node of the nonpolar continuum.

In the DEM models, the physical size of the corn grains was used to model the particles. This lead to run times which are comparable to MPM run times. To model materials with relatively small particles such as sand, it would require a large number of particles and much more computing time. On the other hand, the continuum method with the same mesh size should still yield good results. With modern computing power, no more than 250 000 to 500 000 DEM particles can be modelled with a single processor (Itasca, 2003). New developments in parallel processing can, however solve this problem.

Model	Run time	Number of particles	Initial DOF
DEM	2.92 h	5348	-
Nonpolar MPM: symmetric	1.78 h	8 000	4011
Nonpolar MPM: full geometry	6.83 h	16 000	8022
Polar MPM: symmetric	2.65 h	8 000	6102
Polar MPM: full geometry	10.70 h	16 000	11983

Table 4. Run time to model 10 seconds of silo discharge

6. CONCLUSION

Experiments of silo discharge were performed using corn and sand. The mass flow rate was measured during the discharge process and the flow patterns observed. DEM and MPM (nonpolar and polar) simulations were performed.

A procedure was proposed for determining the corn micro properties needed for DEM simulations. Experimental and numerical shear tests and confined

compression tests were used as part of the calibration process. A unique set of particle friction values and particle stiffness values could be obtained. The calibrated properties were then used for silo modelling. The results show that DEM predicts a flow rate higher than the measured rate for all tests. The flow patterns were, however, qualitatively accurate.

MPM, using a polar and nonpolar Drucker-Prager constitutive model, was used to model both corn and sand. The material properties were obtained from shear and compression tests. Nonpolar MPM was found to predict the flow rate the most accurately, and polar MPM predicted flow rates too high in all tests. The reason for this might be the choice of Cosserat parameters. In addition to the classic parameters such as Young's modulus and Poisson's ratio, other parameters such as the Cosserat shear modulus, moment of inertia and other constitutive parameters are needed. In this study, the standard set of constitutive parameters was used. It is not a straight forward exercise to determine these parameters experimentally, and the effect of the different parameters on the material behaviour needs more research.

When a relatively small number of particles were used in the DEM simulations, computing times were found to be comparable to that of MPM. When larger systems are modelled with much more particles (100 000+), it is expected that it would be advantageous to use MPM instead of DEM in terms of computing times.

In future research, the MPM code will be extended to axisymmetry and three-dimensions. A more detailed study can then be conducted including the geometry of the silo, the effect of inserts on the material flow, and the pressure distribution on the silo walls.

It is concluded that DEM and MPM can successfully model the complete discharge process in terms of flow patterns, flow rate and large deformation. This process is difficult to model with conventional FEM due to severe distortion of the mesh which is a direct result of the large deformations.

7. REFERENCES

1. Yang, A.-C., Hsiau, S.-S., 2001, The simulation and experimental study of granular materials discharged from a silo with the placement of inserts, *Powder Technology*, 120, 244–255.
2. Brown, C., Lahlouh, E., Rotter, J., 2000, Experiments on a square planform steel silo, *Chemical Engineering Science*, 55, 4399–4413.
3. Masson, S. and Martinez, J., 2000, Effect of particle mechanical properties on silo flow and stress from

- distinct element simulations, *Powder Technology*, 109, 164–178.
4. Martinez, M., Alfaro, I., Doblare, M., 2002, Simulation of axisymmetric discharging in metallic silos. analysis of the induced pressure distribution and comparison with different standards, *Engineering Structures*, 24, 1561–1574.
 5. Karlsson, T., Klisinski, M., Runesson, K., 1998, Finite element simulation of granular material flow in plane silos with complicated geometry, *Powder Technology*, 99, 29–39.
 6. Itasca, 1999, PFC^{2D} Theory and Background, Version 2.0, www.itascacg.com.
 7. Coetzee C.J., 2004, The modelling of granular flow using the Particle-in-cell method, Phd Thesis, Department of Mechanical Engineering, University of Stellenbosch.
 8. Belytschko, T., Krongauz, Y., Organ, D., Flemming, M., Krysl, P., 1996, Meshless methods: An overview and recent developments, Report, Northwestern University.
 9. Wieckowski Z., 2002, The dynamic analysis of large strain problems by the material point method, Fifth World Congress on Computational Mechanics, WCCM V, TU Vienna, Austria, July, 7-12.
 10. Sulsky, D., Zhou, S.J. and Schreyer, H.L., 1995, Application of a particle-in-cell method to solid mechanics, *Computer Physics Communications*, 87, 236–252.
 11. Benson, D., 1992, Computational methods in Lagrangian and Eulerian hydrocodes, *Computer Methods in Applied Mechanics and Engineering*, 99, 235–394.
 12. Bardenhagen S.G., Brackbill J.U., Sulsky D.L., 2000, The material-point method for granular materials, *Computational Methods in Applied Mechanics and Engineering*, 187, 529–541.
 13. Herrmann H., 1999, Institute for Computer Applications: Physics on Supercomputers, University of Stuttgart, ICA1 Annual Report.
 14. Eringen C.A., 1999, *Micro-continuum Field Theories, I: Foundations and Solids*, Springer, New York.
 15. de Borst R., 1991, Simulation of strain localization: A reappraisal of the Cosserat continuum, *Engrg. Comput.* 8, 317–332.
 16. Cundall P.A., Strack O.D.L., 1979, A discrete numerical method for granular assemblies, *Geotechnique* 29, 47–65.
 17. Franco Y, Rubinstein D, Shmulevich I., 2005, Determination of discrete element model parameters for soil-bulldozer blade interaction., Proceedings of the 15th international conference of the ISTVS, Hayama, Japan, September 25-29.
 18. Asaf Z, Rubinstein D, Shmulevich I., 2005, Determination of discrete element model parameters using in-situ tests and inverse solution techniques, Proceedings of the 15th international conference of the ISTVS, Hayama, Japan, September 25-29.
 19. Vu-Quoc L., Zhang X., Walton O.R., 2000, A 3-D discrete-element method for dry granular flows of ellipsoidal particles, *Computational Methods in Applied Mechanics and Engineering*, 187, 483-528.
 20. Tanaka H., Momozu M., Oida A., Yamazaki M., 2000, Simulation of soil deformation and resistance at bar penetration by the distinct element method, *Journal of Terramechanics*, 37, 41-56.
 21. Head K.H., 1988, *Manual of Soil Laboratory Testing, Volume 2: Permeability, Shear Strength and Compressibility Tests*, Pentech Press, London, England.
 22. Lambe, T.W., Whitman, R.V., 1969, *Soil Mechanics*, John Wiley & Sons, Inc., New York.
 23. Reimbert M.L., Reimbert A.M., 1976, *Silos, Theory and Practice*, Trans Tech Publications, Clausthal, Germany.
 24. FLAC, 1998, *Fast Lagrangian Analysis of Continua: Theory and Background*, www.itascacg.com.
 25. Tejchman J., 1997, Modelling of shear localisation and autogeneous dynamic effects in granular bodies, des Institutes fur Bodenmechanik und Felsmechanik der Universitat Fridericiana in Karlsruhe.
 26. Vermeer P.A., de Borst R., 1984, Non-associated plasticity for soils, concrete and rock, *Heron* 29(3), 317–332.
 27. Itasca, 2003, PFC3D: User Manual, Optional Features, Version 3.0, www.itascacg.com.
 28. Hassenpflug W.C., 1993, Matrix tensor notation Part I: Rectilinear orthogonal coordinates. *Comput. Math. Appl.*, 26(3), 55–93.
 29. Burgess D., Sulsky D., Brackbill J.U., 1992, Mass matrix formulation of the FLIP particle-in-cell method. *Journal of Computational Physics*, 103, 1–15.
 30. Sulsky D., Chen Z., Schreyer H.L., 1994, A particle method for history-dependent materials, *Comput. Methods Appl. Mech. Engrg.*, 118, 179–196.
 31. Wieckowski Z., 2001, Analysis of granular flow by the material point method, In European Conference on Computational Mechanics, June 26-29, Cracow, Poland.

32. Chen Z., Hu W., Shen L., Xin X., Brannon R., 2002, An evaluation of the MPM for simulating dynamic failure with damage diffusion. *Engineering Fracture Mechanics*, 69, 1873–1890.
33. Borelli, A., Chong, K., 2000, *Elasticity in Engineering Mechanics*, 2nd Edition, John Wiley & Sons, Inc., New York.
34. Mindlin, R.D., 1964, Micro-structure in linear elasticity, *Arch. Rational Mech. Anal.*, 16, 51–78.
35. Dietsche, A., Steinmann, P., William, K., 1993, Micropolar elastoplasticity and its role in localization, *International Journal of Plasticity*, 9, 813–831.

APPENDIX A: The Material-Point Method

The basic MPM formulation based on the classic nonpolar continuum theory is presented. For a detailed description of MPM based on the Cosserat polar continuum, see Coetzee (2004). In the first part of this section, index notation is used to denote vectors and matrices. The subscripts i, j and k are used, assuming values of 1, 2 and 3, unless stated otherwise. In the latter part of the section, Hassenpflug (1993) notation is used. A column vector is indicated by an overbar, \bar{x} , a row vector by an underbar, \underline{x} and a matrix by both, $\bar{\underline{x}}$. Plane strain conditions are assumed.

A.1 Space Discretisation

First, the initial configuration of the body is divided into a number of subregions. This is done as depicted in Figure A.1. In the centre of each subregion a material point or particle is placed. This material point represents the subspace, and is given a mass m_p . The mass is calculated by assuming that the whole mass of the subregion is concentrated at the material point. The mass of a material point is constant and does not change with time or position.

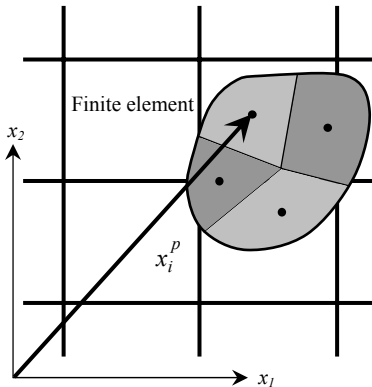


Figure A.1. MPM mass representation, finite elements and modelled body

The density $\rho(x_i)$ represented by this collection of discrete mass points is approximated using the Dirac delta function,

$$\rho(x_i) = \sum_{p=1}^{N_p} m_p \delta(x_i - x_i^p) \quad \text{A.1}$$

where x_i is an arbitrary position vector, x_i^p is the position vector at material point p , N_p is the total number of material points and the Dirac delta function is defined as follows

$$\delta(x-a) = \begin{cases} 0 & x \neq a \\ \infty & x = a \end{cases} \quad \text{and} \quad \int_{-\infty}^{\infty} \delta(x-a) dx = 1 \quad \text{A.2}$$

For clarity, the equations of motion are derived for a single element only. The whole system would be analysed by assembling the matrices and vectors as in standard FEM routines. The mass of each material point is fixed which ensures mass conservation. The weak form of the linear momentum equation is given by

$$\int_V \rho \frac{dv_i}{dt} w_i dV = \int_V \rho f_i w_i dV - \int_V \rho \sigma_{ij}^s w_{i,j} dV + \int_S \tau_i w_i dS \quad \text{A.3}$$

where v_i is the velocity vector, f_i the body forces and τ_i the surface traction acting on surface S and w_i is the test function. σ_{ij}^s is the specific stress tensor defined as the Cauchy stress tensor divided by the material density. Substitution of the discrete density representation, Equation A.1, into Equation A.2 and making use of the definition of the Dirac delta function yields a discrete expression where the integration is performed as a sum of material point properties.

$$\sum_{p=1}^{N_p} m_p \frac{dv_i^p}{dt} w_i^p = \sum_{p=1}^{N_p} m_p f_i^p w_i^p - \sum_{p=1}^{N_p} m_p \sigma_{ij}^{sp} w_{i,j}^p + \int_S \tau_i w_i dS \quad \text{A.4}$$

The superscript p indicates a variable evaluated at the material point. For example, the specific stress

$$\sigma_{ij}^{sp} \equiv \sigma_{ij}^s(x_i^p).$$

A.2 Element Formulation

The element mesh used is similar to that of FEM. Four noded quadrilateral elements are used. Under the assumption of two-dimensional conditions, the acceleration field $\dot{v}_i \equiv \frac{dv_i}{dt}$, for example, can be written in terms of nodal- and shape function-values

$$\dot{v}(\bar{x}, t) \equiv [\dot{v}_1 \quad \dot{v}_2]^T = \bar{N} \dot{\bar{v}}^n \quad \text{A.5}$$

where \bar{N} is a matrix containing the shape functions.

The element nodal acceleration vector, $\dot{\bar{v}}^n$, contains

the nodal values of the acceleration field. The same can be applied to the vector field w_i to obtain a nodal vector \bar{w} . Define the following vectors under plane strain conditions,

$$\bar{\sigma}^s \equiv \begin{bmatrix} \sigma_{11}^s \\ \sigma_{22}^s \\ \sigma_{12}^s \end{bmatrix}, \quad \bar{f} \equiv \begin{bmatrix} f_1 \\ f_2 \end{bmatrix}, \quad \bar{\tau} \equiv \begin{bmatrix} \tau_1 \\ \tau_2 \end{bmatrix} \quad \text{A.6}$$

with $\sigma_{12}^s = \sigma_{21}^s$. Note that under the assumption of plane strain, the third normal stress component σ_{33}^s is not included in the definition above. This component is, however, calculated at each material point and used in the constitutive model. Using these definitions, Equation A.4 can be written as follows

$$\bar{w}^T \sum_{p=1}^{N_p} m_p \left(\bar{N}^p \right)^T \bar{N}^p \dot{\bar{v}}^n = \bar{w}^T \sum_{p=1}^{N_p} m_p \left(\bar{N}^p \right)^T \bar{f}^p - \bar{w}^T \sum_{p=1}^{N_p} m_p \left(\bar{B}^p \right)^T \bar{\sigma}^{sp} + \bar{w}^T \int_S \left(\bar{N}^p \right)^T \bar{\tau} dS \quad \text{A.7}$$

where the superscript p indicates values to be evaluated at the material points. The arbitrary test vector w appears in all the above terms and can thus be dropped. The final discretised system of equations follows as

$$\bar{M} \dot{\bar{v}}^n = \bar{F}^{\text{int}} + \bar{F}^{\text{ext}} \quad \text{A.8}$$

where the mass matrix \bar{M} is given by

$$M_{ij} \equiv \bar{M} = \sum_{p=1}^{N_p} m_p \left(\bar{N}^p \right)^T \bar{N}^p \quad \text{A.9}$$

the internal force vector is given by

$$F_i^{\text{int}} \equiv \bar{F}^{\text{int}} = - \sum_{p=1}^{N_p} m_p \left(\bar{B}^p \right)^T \bar{\sigma}^{sp} \quad \text{A.10}$$

and the external force vector is given by

$$F_i^{\text{ext}} \equiv \bar{F}^{\text{ext}} = \int_S \left(\bar{N}^p \right)^T \bar{\tau} dS \quad \text{A.11}$$

The matrix \bar{B}^p contains shape function gradients. In practice, to simplify computations, a lumped mass matrix may be used instead of the consistent mass matrix given by Equation A.9. The lumped mass matrix is a diagonal matrix with each entry being the corresponding row sum of the consistent mass matrix. Matrix inversions become trivial if a lumped matrix is used, at the cost of introducing a small amount of numerical dissipation (Burgess et al., 1992, Bardenhagen et al., 2000). The consistent mass matrix can also be singular for certain arrangements of the particles. There appears to be only a few arrangements of particles that yield a singular consistent mass matrix, but nearby arrangements might result in an ill-

conditioned matrix. On the other hand, the lumped matrix is diagonal and well conditioned.

A.3 Time Integration

Let the time step size be Δt . The solution to the system of Equations A.8 is found at discrete instants in time t , $t+1$, . . . , $t+n$. The calculation during each time increment consists of three phases; a initialisation phase, a Lagrangian phase and a convective phase (Sulsky et al., 1994).

A.3.1 Initialisation Phase

Assume that the position and velocity vector, stress tensor, strain tensor and history dependent variables of each material point are known at time t . With the position of each particle known, its shape function values can be computed and hence the mass matrix, \bar{M}^t , given by Equation A.9. Mapping of the particle velocities to the nodes, provides the initial data for the solution to Equation A.8. The following equation is solved to obtain the nodal velocity $\bar{v}^{n,t}$ at time t .

$$\bar{M}^t \bar{v}^{n,t} = \sum_{p=1}^{N_p} m_p \left(\bar{N}^{p,t} \right)^T \begin{bmatrix} v_1^{p,t} \\ v_2^{p,t} \end{bmatrix} \quad \text{A.12}$$

where $\begin{bmatrix} v_1^{p,t} & v_2^{p,t} \end{bmatrix}^T$ is the material point velocity vector at time t , containing the velocity components in the x_1 - and x_2 -directions respectively. This equation expresses equivalence of momentum calculated for the material points and for the nodes (Wieckowski, 2001).

A.3.2 Lagrangian Phase

With the value of the shape functions known at each particle position, the internal- and external-force vectors can be calculated using Equations A.10 and A.11 respectively. With these two vectors and the mass matrix known, Equation A.8 is solved for the nodal acceleration at time t .

$$\dot{\bar{v}}^{n,t} = \left(\bar{M}^t \right)^{-1} \left(\bar{F}^{\text{int},t} + \bar{F}^{\text{ext},t} \right) \quad \text{A.13}$$

The "new" nodal velocity, $\bar{v}^{n,t+1}$, at time $t+1$ is obtained by using an explicit time integrator

$$\bar{v}^{n,t+1} = \bar{v}^{n,t} + \Delta t \dot{\bar{v}}^{n,t} \quad \text{A.14}$$

which obviously requires very small time steps to ensure accuracy and stability. Using the new nodal velocity, the increment in strains can be calculated at the particles. Define the vector of strain increment as follows

$$\Delta \bar{\epsilon}^p \equiv \begin{bmatrix} \epsilon_{11}^p & \epsilon_{22}^p & \epsilon_{12}^p \end{bmatrix}^T \quad \text{A.15}$$

This vector can be calculated using matrix $\bar{B}^{p,t}$

$$\Delta \bar{\varepsilon}^{p,t+1} = \Delta t \bar{B}^{p,t} \bar{v}^{n,t+1} \quad \text{A.16}$$

With the increment in strain known, the new stress state $\bar{\sigma}^{p,t+1}$ at each material point can be calculated based on the chosen constitutive model. One way of doing this, would be to calculate the stress increment, using the tangent modulus $\bar{T}^{p,t}$,

$$\Delta \bar{\sigma}^{p,t+1} = \bar{T}^{p,t} \Delta \bar{\varepsilon}^{p,t+1} \quad \text{A.17}$$

The use of the tangent modulus in a numerical algorithm, however, results in a tendency for the stress to drift from the yield surface (Sulsky et al., 1995). In practice an incremental iterative scheme is rather used. With the given increment in strain, the material is assumed to be elastic, and a trial stress state is computed. The yield function f is evaluated using the trial state, and if $f \leq 0$ the material point is still in the elastic region and no further calculations are needed. However, if $f > 0$, return algorithms, based on the flow potential g , are needed to force f back to zero. In the case of a Mohr-Coulomb or Drucker-Prager model, a simple one-step return to the yield surface is possible (FLAC, 1998). For other models like Lade, an iterative procedure is needed.

History dependent variables such as strain-hardening parameters may also be updated at this stage. During the Lagrangian phase the nodes are assumed to move at the computed nodal velocity $\bar{v}^{n,t+1}$. Thus, points in the interior of the element move in proportion to the motion of the nodes, as given by the representation using the nodal shape functions. Since shape functions are used to map the nodal velocity continuously to the interior of the element, the positions of the material points are updated by moving them in a single-valued, continuous velocity field. Similarly, the velocity of a material point is updated by mapping the nodal accelerations to the material point position. The updated position vector and velocity vector follow as

$$\begin{aligned} \bar{x}^{p,t+1} &= \bar{x}^{p,t} + \Delta t \bar{N}^{p,t} \bar{v}^{n,t+1} \\ \bar{v}^{p,t+1} &= \bar{v}^{p,t} + \Delta t \bar{N}^{p,t} \bar{a}^{n,t+1} \end{aligned} \quad \text{A.18}$$

Because the velocity field is single-valued, interpenetration of material is precluded. This feature of the algorithm allows simulations of impact and penetration without the need for a special contact algorithm.

A.3.3 Convective Phase

At this point in the computational cycle, the material points are completely updated and carry the complete solution, i.e., all the state variables needed to start a new calculation step are carried by the material points. During the convective phase, the material points are held fixed and the element mesh can be redefined. The mesh can be chosen in any convenient manner, for example adaptive meshes can be used to resolve sharp gradients and interfaces. The simplest and most convenient choice is, however, to keep the existing mesh. Any motion of the mesh relative to the material points model convection. Since the material points do not move during the convective phase, material point properties have the same value at the end of the convective phase as they had at the end of the Lagrangian phase. This completes the computational cycle. A new cycle is begun using the information carried by the material points to initialise nodal values on the element mesh.

A.4 Stability

In the previous sections, a simple explicit time integrator is used of which the time step should satisfy the stability condition, i.e. the critical time step should be the smallest ratio of the element size to the wave speed through the material. For small displacements, the spatial discretisation in MPM is equivalent to that of FEM using Gauss points at the same locations as those of the material points in each element. Therefore, the convergence behaviour of the integrator used is similar to that employed to integrate the corresponding equations in FEM. However, according to Chen et al. (2002), no consistent theoretical results have been obtained for the convergence behaviour of time integrators when larger deformations occur and a reasonable time step is usually found through numerical experiments.

A.5 Contact Model

The MPM formulation presented here automatically enforces no-slip contact between two different bodies. The reason for this is that a single-valued velocity field is used for updating the particle positions. Bardenhagen et al. (2000), however, developed an algorithm which relaxes the no-slip condition and allows Coulomb friction and slip at contacting boundary nodes. This contact algorithm was implemented to model the silo wall-material interface. The theory behind the contact model is not presented here and the reader is referred to Bardenhagen et al. (2000) and Coetzee (2004).

APPENDIX B: The Cosserat Polar Continuum

In a theory of deformation of continua by E. Cosserat and F. Cosserat in 1909, the couple per unit area (couple-stresses), acting across a surface within a material volume or on its boundary, is taken into account in addition to the usual force per unit area, ΔS . Similar to the *classic stress vector*, the *couple stress vector* μ_i is defined by

$$\mu_i = \lim_{\Delta S \rightarrow 0} \frac{\Delta M_i}{\Delta S} \quad \text{B.1}$$

where M_i is the couple vector which can result from a magnetic field or inter-particle action. Figure B.1 shows the stress and couple stress components acting simultaneously at a point in the continuum.

The presence of the couple stresses does not affect the linear momentum principle; hence the equations of motion of the nonpolar continuum still applies,

$$\rho \frac{dv_i}{dt} = \rho f_i + \sigma_{ij,j} \quad \text{B.2}$$

where v_i is the velocity vector, f_i the body force per unit volume and σ_{ij} the stress tensor. The moment of momentum equation of the nonpolar continuum is given by,

$$\int_S \varepsilon_{ijk} x_j \sigma_k dS + \int_R \varepsilon_{ijk} x_j f_k \rho dV = \frac{d}{dt} \int_R \rho \varepsilon_{ijk} x_j v_k dV \quad \text{B.3}$$

where ε_{ijk} is the permutation symbol and x_j the position vector.

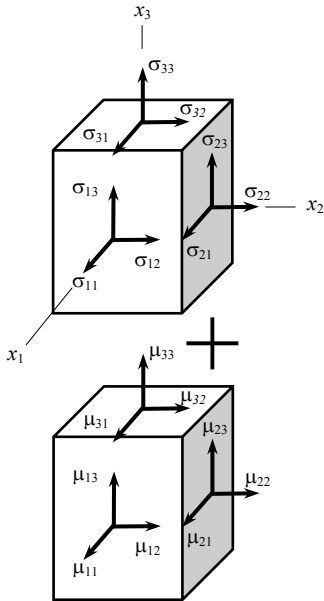


Figure B.1. Stress tensor and couple stress tensor components

This equation states that the stress tensor is symmetric, and when this is enforced, the momentum equation does not have to be solved explicitly.

For a polar continuum, the momentum equation however needs to be revised. Firstly, the body moment c_i per unit mass and the moment per unit area μ_i are introduced in addition to the moments of the body force per unit mass f_i and the surface force per unit area σ_i . Secondly the *spin angular momentum* $h_i^c = J\omega_3^c$ (per unit mass) needs to be included,

$$\int_S (\varepsilon_{ijk} x_j \sigma_k + \mu_k) dS + \int_R \rho (\varepsilon_{ijk} x_j f_k + c_i) dV = \frac{d}{dt} \int_R \rho (\varepsilon_{ijk} x_j v_k + h_i^c) dV \quad \text{B.4}$$

Making use of $\sigma_k = \sigma_{kr} n_r$ and Gauss's theorem, the above equation reduces to

$$\varepsilon_{ijk} \sigma_{kj} + u_{ij,j} + \rho c_i = \rho \frac{dh_i^c}{dt} \quad \text{B.5}$$

The kinematics of polar continua are characterised by rotational degrees of freedom $w_i^c \rightarrow \mathfrak{R}^3$, which are independent of the translatory motion described by the displacement field, u_i . Thus the field of continuum macro rotations does no longer coincide with that of micro rotations at each material particle. In other word, the Cosserat micro rotation w_i^c differs from the classical macro rotation w_i since three rotational degrees-of-freedom are introduced in addition to the conventional three translational degrees-of-freedom.

Assign a local rigid triad to every material point of the continuum body. The symmetric linear strain tensor is given by

$$e_{ij} = \frac{1}{2} \left[\frac{\partial u_i}{\partial x_j} + \frac{\partial u_j}{\partial x_i} \right] \quad \text{B.6}$$

and the skew-symmetric linear rotation tensor by

$$w_{ij} = \frac{1}{2} \left(\frac{\partial u_i}{\partial x_j} - \frac{\partial u_j}{\partial x_i} \right) \quad \text{B.7}$$

The rotation vector is given by

$$w_i = \frac{1}{2} \varepsilon_{ijk} w_{kj} \quad \text{B.8}$$

For the formulation of constitutive relationships, deformation measures which are invariant with respect to rigid body motion are needed. In the Cosserat theory, two other deformation measures are introduced, namely

$$\Omega_k = w_k - w_k^c \quad \text{B.9}$$

which represents the relative rotation between the material element and the corresponding rigid coordinate cross, and

$$\kappa_{ij} = w_{i,j}^c \quad \text{B.10}$$

which is a measure for the relative rotation between neighbouring rigid crosses (curvature). Figure B.2 shows the two-dimensional (planar deformation) formulation of the Cosserat continuum.

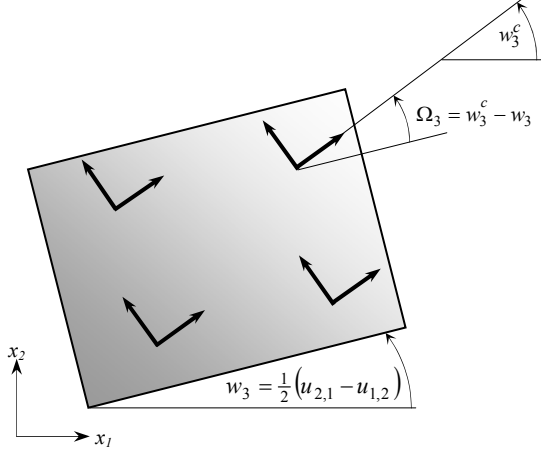


Figure B.2. Rotated state in a Cosserat continuum

Equations B.6 and B.9 can be combined into a single, tensorial deformation measure, namely

$$\lambda_{ij} = u_{i,j} + \varepsilon_{ijk} w_k^c \quad \text{B.11}$$

This “relative deformation or strain” tensor can now be decomposed into symmetric and skew-symmetric components.

$$\begin{aligned} \lambda_{ij} &= \lambda_{ij}^{sym} + \lambda_{ij}^{skw} \\ &= \left[\frac{1}{2} (u_{i,j} + u_{j,i}) \right] + \left[\frac{1}{2} (u_{i,j} - u_{j,i}) + \varepsilon_{ijk} w_k^c \right] \\ &= [e_{ij}] + [w_{ij} + w_{ji}^c] \quad \text{B.12} \\ &= [e_{ij}] + [w_{ij} - w_{ij}^c] \\ &= e_{ij} + \Omega_{ij} = \frac{1}{2} (\lambda_{ij} + \lambda_{ji}) + \frac{1}{2} (\lambda_{ij} - \lambda_{ji}) \end{aligned}$$

The symmetric part reduces to the linear macro strain tensor and the skew-symmetric part is the relative rotation. The shear deformation λ_{ij} can be interpreted as depicted in Figure B.3.

The relation between micro curvature and couple stresses is depicted in Figure B.4 for the two-dimensional case (Boresi and Chong, 2000). Mindlin (1964) calls the micro curvature the macro gradient of the micro deformation. Where the application of shear stresses causes the material to deform as depicted in Figure B.3, the couple stresses cause the material to deform as shown in Figure B.4.

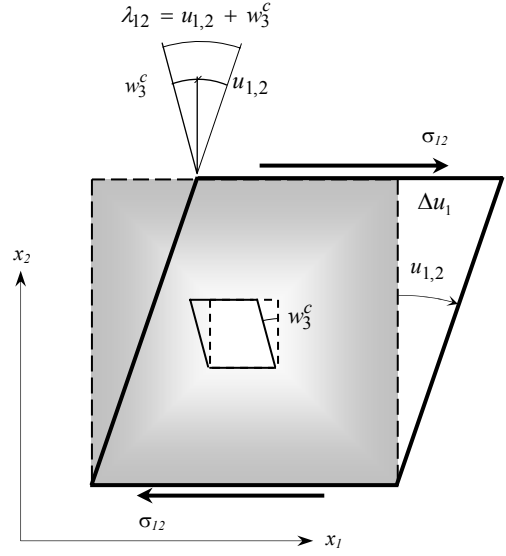


Figure B.3. Interpretation of the shear stress deformations in a Cosserat continuum

The rigid triad at the lower left-hand corner rotates by w_3^c while the triad at the lower right-hand corner

rotates by $w_3^c + \left(\frac{\partial w_3^c}{\partial x_1} \right) dx_1$. Thus, the relative rotation

is, as shown, $\left(\frac{\partial w_3^c}{\partial x_1} \right) dx_1$. Using the relation between

arc length, radius and the angle, it can easily be shown that the radius R_{31} is the inverse of the curvature κ_{31} .

The curvatures describe the kinematic field quantities that are energetically conjugate to the couple stresses (Dietsche et al., 1993).

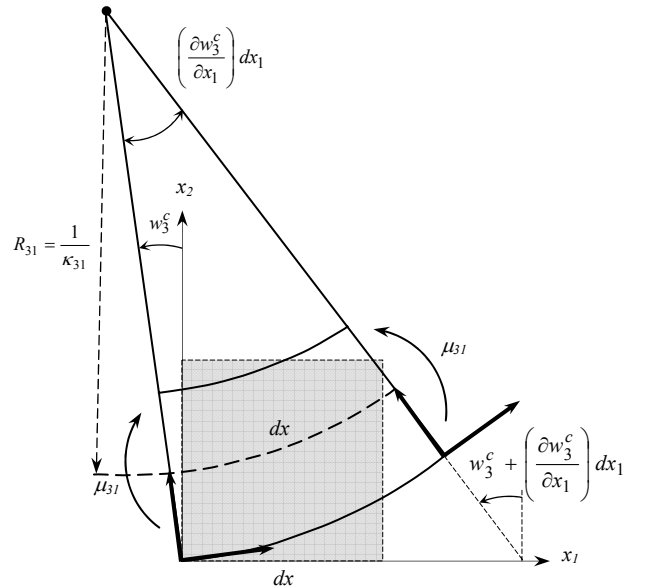


Figure B.4. Definition of curvatures in a Cosserat continuum